JOURNAL OF SYNCHROTRON RADIATION

ISSN 1600-5775

Depth-dependent atomic valence determination by synchrotron techniques

Robbyn Trappen,[a] Jinling Zhou,[a] Vu Thanh Tra,[b] Chih-Yeh Huang,[c] Shuai Dong,[d] Ying-Hao Chu[b,e] and Mikel B. Holcomb[a]*

[a]Department of Physics and Astronomy, West Virginia University, Morgantown, WV 26506, USA, [b]Department of Materials Science and Engineering, National Chiao Tung University, 30010 HsinChu, Taiwan, [c]Department of Mechanical and Aerospace Engineering, West Virginia University, Morgantown, WV 26506, USA, [d]Department of Physics, Southeast University, Nanjing 211189, People's Republic of China, and [e]Institute of Physics, Academia Sinica, 105 Taipei, Taiwan. *Correspondence e-mail: mikel.holcomb@mail.wvu.edu

Received 2 May 2018
Accepted 20 August 2018

Edited by A. F. Craievich, University of São Paulo, Brazil

Keywords: X-ray absorption; valence; manganites; thin films; Hamiltonian calculations.

Supporting information: this article has supporting information at journals.iucr.org/s

The properties of many materials can be strongly affected by the atomic valence of the contained individual elements, which may vary at surfaces and other interfaces. These variations can have a critical impact on material performance in applications. A non-destructive method for the determination of layer-by-layer atomic valence as a function of material thickness is presented for $La_{0.7}Sr_{0.3}MnO_3$ (LSMO) thin films. The method utilizes a combination of bulk- and surface-sensitive X-ray absorption spectroscopy (XAS) detection modes; here, the modes are fluorescence yield and surface-sensitive total electron yield. The weighted-average Mn atomic valence as measured from the two modes are simultaneously fitted using a model for the layer-by-layer variation of valence based on theoretical model Hamiltonian calculations. Using this model, the Mn valence profile in LSMO thin film is extracted and the valence within each layer is determined to within an uncertainty of a few percent. The approach presented here could be used to study the layer-dependent valence in other systems or extended to different properties of materials such as magnetism.

1. Introduction

The valence of atoms often has a strong effect on the properties of materials, such as magnetism (Gerber *et al.*, 2015), conductivity (Duba & Nicholls, 1973) and superconductivity (Holmes *et al.*, 2007). The atomic valence is often perturbed at the surface and/or interface and this deviation may play a strong role in many physical phenomena such as interfacial coupling (Zhou *et al.*, 2015) and dead layers (Li *et al.*, 2012; Wang *et al.*, 2010). It should be noted that the exact definition for atomic valence has been used in different ways, once meaning the maximum number of bonds an element could form. The terms valence and oxidation state are sometimes used interchangeably. The former relates to the average number of outer electrons around each element, and the latter to the number of electrons that are added or taken away when bound to other elements in a crystal structure. Even the use of the term valence, in some sense, represents a chemist's viewpoint. An alternative language, which corresponds to a physicist's viewpoint, brings to the fore the microscopic mechanisms responsible for the position-dependent occupancy and describes this feature in terms of band-bending near surfaces and interfaces (Butler *et al.*, 2014; Batzill, 2006) as well as position-dependent electronic correlations.

There are several approaches that researchers currently utilize to investigate the atomic valence of atoms. X-ray

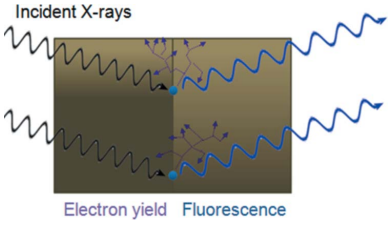

photoelectron spectroscopy (XPS) and X-ray absorption spectroscopy (XAS) can give a very accurate valence over their varying surface-probing depths. Cross-sectional transmission electron microscopy (TEM) images can even map the valence across the thickness of the samples. While TEM might still be an ideal approach for probing the valence slowly varying through the individual atomic layers, the resolution for some elements is often limited (typically 1 eV without an electron monochromator) (Egerton, 2009) and the result can be obscurely influenced by the measurement preparation (Bals *et al.,* 2007).

Here, we present a non-destructive approach of combining two absorption detection modes, electron yield and fluorescence, with different probing depths to map out the layer-by-layer valence of a thin film. While laboratory-based techniques (rather than synchrotron facilities) could also be utilized for the depth-dependent determination of valence, we do take advantage of the high flux and energy resolution available at several beamlines at the Advanced Light Source at Lawrence Berkeley National Laboratories. We have previously used this method to study the Mn valence in $La_{0.7}Sr_{0.3}MnO_3$/$PbZr_{0.2}Ti_{0.8}O_3$ (LSMO/PZT) heterostructures in order to better understand the charge mechanisms in the magnetoelectric coupling in this bilayer system (Zhou *et al.,* 2015), and also in LSMO thin films alone in order to understand the change in valence near the surface and interface of the films caused by polar discontinuity (Trappen *et al.*, 2018). Here, we will focus on illustrating the experimental and modeling approach for investigating atomic valence using LSMO thin films grown on strontium titanate substrates with (001) orientation. This general procedure could also be extended to depth-dependent magnetic measurements, using a similar approach taking advantage of surface and bulk methods such as circular dichroism, vibrating sample magnetometry or magneto-optical Kerr measurements.

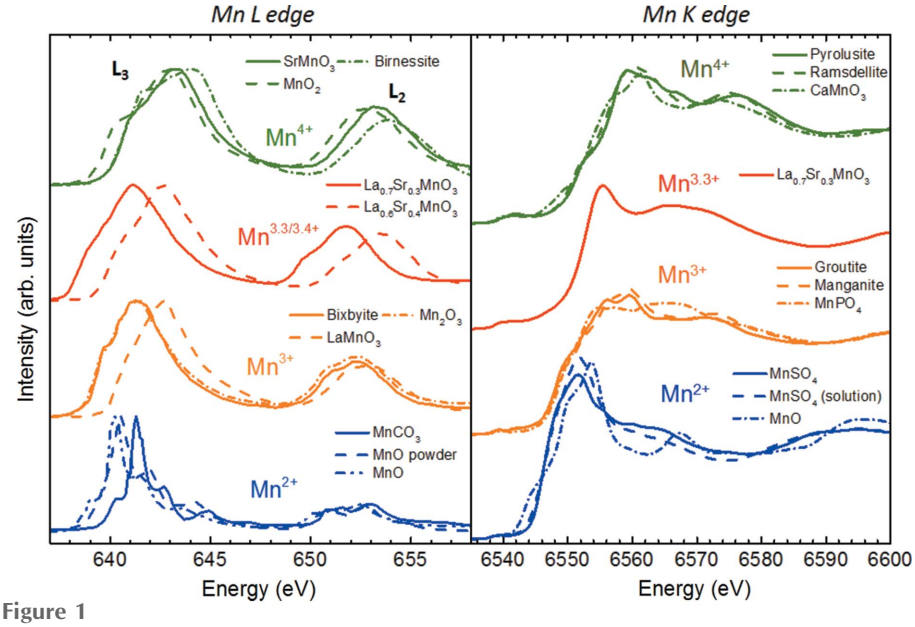

Figure 1
References used for linear combination fits for the Mn *L* edge (left) and *K* edge (right). The spectra shown correspond to the references that produced the best fit to our data. *K*-edge spectra are taken from Manceau *et al.* (2012) and the rest of the *L*-edge spectra are extracted from Pecher *et al.* (2003), Khan (2015), Alonso *et al.* (2007), Kim *et al.* (2015), Gilbert *et al.* (2003) and Pellegrin *et al.* (1997).

(Manceau *et al.,* 2012) and *L* edge (Pecher *et al.,* 2003; Khan, 2015; Alonso *et al.,* 2007; Kim *et al.,* 2015; Gilbert *et al.,* 2003; Pellegrin *et al.,* 1997). The two distinct peaks in the *L* edge refer to the $2p_{3/2} \rightarrow 3d$ (L_3) and the higher energy $2p_{1/2} \rightarrow 3d$ (L_2) transition and are caused by the spin–orbit splitting of the $2p$ energies. As the valence is determined using a combinatorial approach (Trappen *et al.*, 2018; Manceau *et al.,* 2012), multiple references for each valence species are used.

Shown in Fig. 2 is an example of the fitting of our spectra for 1 u.c. (unit cell) of LSMO for the *K* and *L* edges. The top panels show the spectrum with the fit (solid points and dashed lines) with the residuals below, indicating that the fits reproduce the spectra well with near-noise residuals. The dashed lines show the contributions of each reference, determined by the weights of each spectrum in the linear combination fit.

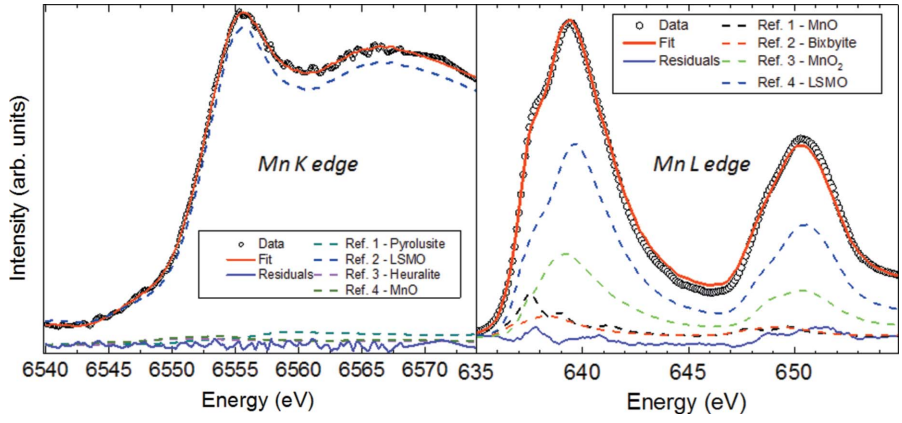

Figure 2
Examples of fits to the Mn *K* edge (left panel) and *L* edge (right panel). Experimental spectral are shown as open points, fits as solid red lines. Residuals are shown at the bottom in solid purple and the contributions of each reference are shown as dashed lines.

2. Experimental methods

To study the valence of Mn, we investigated the XAS at both the Mn *K* and *L* edges. The *L* edge probes the $2p$ energy levels of elements while the *K* edge probes the deeper $1s$ core levels. Fig. 1 shows reference Mn absorption edges for both the *K* edge

Different modes of detection can be utilized to measure these absorption edges. The incident X-rays are absorbed by exciting core electrons to empty states above the Fermi energy, leaving a hole. Recombination of the hole leads to both creation of an X-ray, measured by fluorescence yield (FY), and creation of an Auger electron (de Groot, 2008). As the Auger electron scatters through the material it creates many secondary electrons. Both types of electrons are collected in total electron yield (TEY) mode. The inherent probing depth of these detection modes are illustrated in Fig. 3(*a*).

As X-rays are much less easily scattered than electrons, the two detection modes have very different probing depths, which will also depend on the incident X-ray energy. As it requires more energy to excite an electron from the n = 1 states (K edge) than the n = 2 states (L edge), K-edge absorption requires higher energies and probes deeper into the sample. The energies of the K and L edge (Thompson, 2009) and probing depths for Mn (Henke *et al.,* 1993; Seah & Dench, 1979; Ruosi *et al.,* 2014) are listed in Table 1. It should be noted that these values are estimates, with the exception of the probing depth for L-edge TEY, which was determined specifically for LSMO by Ruosi *et al.* (2014), although the probing depth can be significantly influenced by the material density which varies from sample to sample. We tried various values of the TEY probing depth in order to assess the affect that any variation in its value would have on our modeling and found that it does not significantly affect the results. This is elaborated on further in the supporting information.

The probing depths for the K- and L-edge FY were determined from tabulated X-ray absorption length values (Henke *et al.,* 1993). As the probing depth for TEY is primarily determined by the inelastic mean free path of the electron, the value for TEY of the Mn K edge was estimated using a universal curve presented by Seah & Dench (1979). As the probing depths are dependent on material-specific parameters like density (Henke *et al.*, 1993), there is some small variation in these numbers with different materials; however, the depth sensitivities of the detection modes will be quite similar. The contribution from a specific layer of depth z within the material can be determined by the exponential formula $\exp[-(z/\lambda)]$, where λ is the probing depth of the detection modes (Frazer *et al.,* 2003; Pesquera *et al.,* 2012). Note that fluorescence on transition metal L edges in particular is susceptible to overabsorption (also sometimes referred to as self-absorption) artifacts, which can either be corrected by using angle-dependent measurements (Eisebitt *et al.,* 1993) or avoided by use of inverse partial fluorescence detection (Wadati *et al.,* 2012).

Table 1
Edge energies and probing depths for TEY and FY on the Mn K and L edges.

Edge	Energy (eV)	λ_{TEY} (nm)	λ_{FY} (nm)
K edge	6539	14.8	4000
L edge	638.7	2.6	140

XAS measurements were performed at the Advanced Light Source. Measurement details are reported by Trappen *et al.* (2018). In this study, we have used K-edge FY and L-edge TEY. Given the probing depths listed in Table 1, the exponential curves for the TEY and FY are illustrated in Fig. 3(*b*). The TEY mode at the L-edge is the most surface sensitive of these detection modes because of the small probing depth. Thus, while L-edge TEY would be excellent at determining the Mn valence at the surface, little contribution would come from deep within the sample. On the other hand, FY of the K edge probes many micrometres into the sample; thus, for the measurements of thin films, this detection mode nearly produces a straight average of the valence of all layers. Utilizing two (or more) methods that measure the same property (valence here) with different probing depths can allow one to separate out the depth-dependence of that property if combined with samples of varying thickness.

Depth-dependent methods (Bertacco *et al.,* 2002) have previously been utilized by only changing the incident angle of the incident radiation (rather than using two measurement techniques), thereby changing the effective probe depth. However, the difference in the measurement depth is limited to one over the cosine of the incident angle from the normal of the sample. Some surface-sensitive measurements, such as TEY, are only well optimized for angles less than 60° from the normal of the sample (Ufuktepe *et al.,* 2011), limiting the change in effective measuring depth to a factor of two. This factor of two difference might be sufficient for variation of surface valence, but not if the properties of a buried interface are the goal of the study. For this determination of the valence of a buried layer, a study of layer thickness can be beneficial.

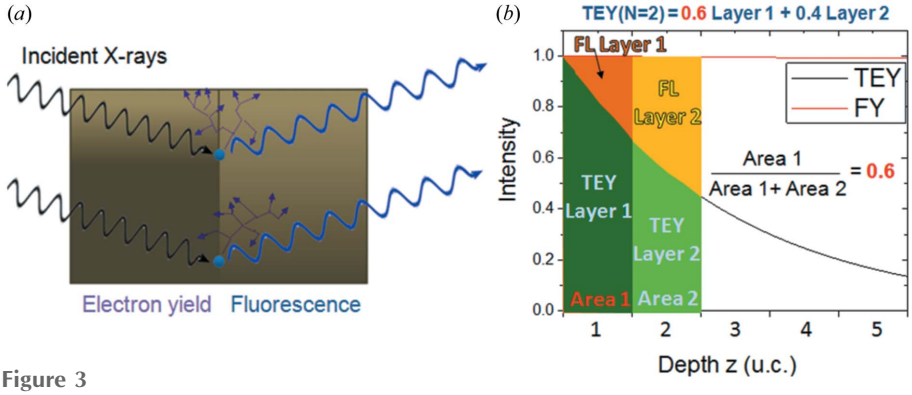

Figure 3
(*a*) Diagram showing the TEY and FY processes. Straight arrows indicate scattered secondary electrons. The brightly shaded areas show the relative probing depths of the two detection modes. Electrons created deeper in the samples are less likely to escape the sample and reach the detector. Photons have longer scattering paths. (*b*) Relative XAS intensity as a function of depth for TEY (black, $\lambda \simeq 1$ nm) and FY (red, $\lambda \simeq 1$ µm). Note that the FY signal is nearly a bulk average over the range of our thin films because of the longer scattering path. As an example, the contribution to the TEY signal for a two-layer film is shown in shaded green areas.

To study the variation of Mn valence with thickness, LSMO thin films were grown on $SrTiO_3$ (STO) substrates by optimized pulsed-laser deposition. The details of growth and characterization are reported elsewhere (Zhou *et al.,* 2015). Multiple samples of different thicknesses were grown in the 1–16 u.c. range. The full set of experimental thickness-dependent valence data were fitted using a standard least-squares optimization method. Here the TEY and FY data were fitted simultaneously. The minimization was performed using a differential evolution algorithm. Differential evolution is particularly well suited for larger parameter spaces like those discussed in this article and is also used, for example, in fitting X-ray reflectivity data (Wormington *et al.,* 1999; Björck & Andersson, 2007), where the number of fit parameters can become large.

3. Results and discussion

The red circle and black square points in Fig. 4 (taken from Trappen *et al.*, 2018) result from fitting our spectra for various sample thicknesses *via* the combinatorial method. The valences obtained from fitting the bulk-sensitive FY spectra are shown as black squares while the valences obtained from the surface-sensitive TEY data are shown as red circles. The light-blue dotted line indicates the expected Mn valence for LSMO of 3.3, which is 3.3 because of the material composition of 70% $LaMnO_3$ (Mn^{3+}) and 30% $SrMnO_3$ (Mn^{4+}). It can be seen that the FY data hover around the expected average value of 3.3 for thicknesses above approximately 4 u.c., below which the valence decreases. The valence obtained from TEY, however, is larger than the bulk value, which would indicate a raised surface valence. Note that the results come closer together for very thin film thicknesses, since both detection modes probe a similar volume in this case.

In order to interpret our experimental valence results, the layer-dependent valence was simulated for LSMO films of varying thickness using a tight-binding (TB) double-exchange model with only *d*-orbitals. The details of our TB model and the numerical details on the solution of this model can be found in our previous publications (Zhou *et al.,* 2015; Dong *et al.,* 2011). Consistent with our TiO_2 terminated substrates, an *n*-type polar interface between STO and LSMO (TiO_2–$La_{1-x}Sr_xO$–MnO_2) is adopted here. In this configuration, the LSMO film is expected to have a MnO_2 termination to be stoichiometrically complete. For best fitting, the dielectric constant of the lattice was chosen as 36 and the polar termination charge was set to +0.975 e per u.c., while other coefficients are identical to previous studies (Dong *et al.,* 2011).

Fig. 5 shows the results of the simulation (open points) and our experimental fits (filled points). The horizontal dotted line indicates the expected Mn valence for LSMO of 3.3. Here, the calculated Mn valence within each plane is shown. For example, the square data point in Fig. 5 corresponds to the Mn valence for a thickness of 1 u.c. in which it is the expected value of 3.3. However, for a thickness of 2 u.c. (open circles), the valence is seen to vary from its bulk value with a valence of 3.55 in the surface layer and 2.9 for the interfacial layer, although the average of the two values is nearly 3.3. A similar trend is observed for samples with other thicknesses.

The calculations indicate that the Mn valence varies substantially from its bulk value near the film surface and interface and returns to its bulk value towards the central layers of the material. This variation is due to charge reconstruction caused by the polar discontinuity at the LSMO/STO interface (as discussed by Trappen *et al.*, 2018). In order to model this change in our own system (and generate the filled points in Fig. 5), we parameterized this trend as a sum of two variations, one from the bulk valence V_{bulk} to some value of the surface valence V_{surf} and one to the interface valence V_{int}. The calculation results were analyzed and found to follow an approximately exponential trend that is given by

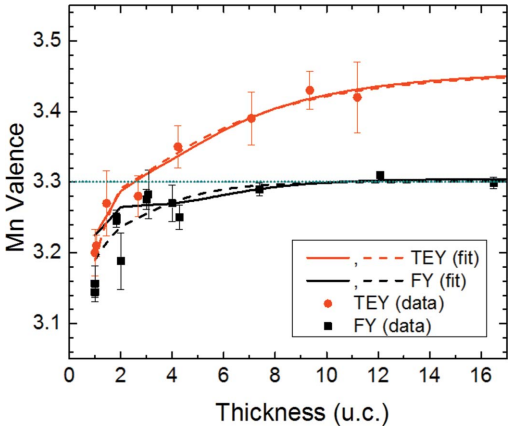

Figure 4
Valence determined from TEY and FY measurements (solid points) and fits (discussed in §3) using depth-dependent models where the surface and interface valence vary (solid lines) and do not (dashed lines) vary with thickness. The horizontal dashed line indicates the bulk Mn valence of 3.3.

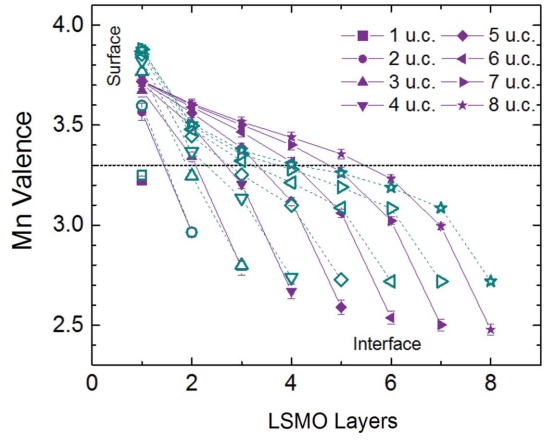

Figure 5
Plane-resolved valence for thicknesses of 1–8 u.c. as determined from theoretical calculations (open points) and by fitting the data (solid points, discussed in §3). For example, the square points refer to the valence of a monolayer film. The round points were calculated for a two unit-cell film, where the higher valence is the calculated surface Mn valence. The horizontal dotted line indicates the expected bulk Mn valence of 3.3.

$$V(z) = \frac{V_{\rm bulk}}{2}\left\{1 - \alpha \exp\left[\frac{-(z-1)}{L_{\rm surf}}\right]\right\} + \frac{V_{\rm bulk}}{2}\left[1 - \beta \exp\left(\frac{z - z_{\rm int}}{L_{\rm int}}\right)\right], \quad (1)$$

where the two coefficients

$$\alpha = \left[2\,\exp\left[(z_{\rm int}-1)/L_{\rm surf}\right]\left(V_{\rm bulk}\left\{\exp\left[(z_{\rm int}-1)/L_{\rm int}\right]-1\right\} + V_{\rm int} - V_{\rm surf}\,\exp\left[(z_{\rm int}-1)/L_{\rm int}\right]\right)\right] \Big/ \left[V_{\rm bulk}\left(\exp\left\{\left[(z_{\rm int}-1)/L_{\rm surf}\right] + \left[(z_{\rm int}-1)/L_{\rm int}\right]\right\} - 1\right)\right], \quad (2)$$

$$\beta = \left[2\,\exp\left[(z_{\rm int}-1)/L_{\rm surf}\right]\left(V_{\rm bulk}\left\{\exp\left[(z_{\rm int}-1)/L_{\rm surf}\right]-1\right\} + V_{\rm surf} - V_{\rm int}\,\exp\left[(z_{\rm int}-1)/L_{\rm surf}\right]\right)\right] \Big/ \left[V_{\rm bulk}\left(\exp\left\{\left[(z_{\rm int}-1)/L_{\rm surf}\right] + \left[(z_{\rm int}-1)/L_{\rm int}\right]\right\} - 1\right)\right] \quad (3)$$

have been obtained by requiring that $V(1) = V_{\rm surf}$ and $V(z_{\rm int}) = V_{\rm int}$, which are parameters to be determined from the fit. The characteristic lengths $L_{\rm surf}$ and $L_{\rm int}$ refer to the depth over which the valence changes from its bulk value $V_{\rm bulk}$ to, for example, 1/e $(V_{\rm bulk} - V_{\rm surf})$. A schematic plot of $V(z)$ is shown in Fig. 6(*a*) for four and eight unit cells. As shown in the inset of Fig. 6(*a*), $z = 1$ is taken to be the surface layer. Note that equations (2) and (3) become infinite when $z_{\rm int} = 1$, *i.e.* a monolayer thickness. As it is impossible to simultaneously satisfy the boundary conditions for both $V_{\rm surf}$ and $V_{\rm int}$, the case of $V(1)$ was set to a constant $V_{\rm mono}$ and included as a fit parameter.

The blue curve in Fig. 6(*b*) shows the fit of the valence for 8 u.c. LSMO thickness to this formula. Instead of an exponential variation, a power-law variation was also tried, which gives nearly the same quality of fit (red curve). However, some problems arose when trying to fit the experimental data to this model because of a large amount of coupling between fit parameters which made a unique solution difficult to determine. This is further discussed in the supporting information.

It is clear that the shape of the points in Fig. 5 do not appear similar to the thickness-dependent trend in Fig. 4 (nor should they). The valence determined from a measurement (shown in Fig. 4) contains contributions from multiple layers in the material (modeled in Fig. 5). Thus, the upward trend in the measured valence with sample thickness refers to the weighted average of the valence, based on the percentage with which each layer contributes to the measured signal. As discussed earlier, the contribution to the signal from a given layer is weighted by a factor $\exp[-(z/\lambda)]$ (Frazer *et al.*, 2003; Pesquera *et al.*, 2012). Additionally, it is necessary to account for the attenuation of the incoming X-rays, denoted by λ_0. For a material consisting of N layers, the measured valence is a weighted sum of the form given in the following equation,

$$V(N) = \frac{\sum_{i=1}^{N} V(i) \int_{i-1}^{i} \exp(-z/\lambda)\exp(-z/\lambda_0)\,{\rm d}z}{\int_{0}^{N} \exp(-z/\lambda)\exp(-z/\lambda_0)\,{\rm d}z}. \quad (4)$$

Here, the integration over z in each numerator term is carried out over the ith unit cell. The denominator is a factor that normalizes the signal from a given layer to the total signal from the whole film, which changes with thickness. For FY mode, $\lambda \simeq \lambda_0 \simeq 1$ µm which is much larger than the thickness of the sample (Table 1), so $V(N)$ is essentially a straight average and the exponential factors are approximately equal to one. For TEY mode, the escape depth of the electrons is of the order of nanometres, so this detection mode is more surface-sensitive. To accurately determine the depth-dependent valence, it is necessary to combine two detection modes with very different probing depths. While the bulk-average signal contains contributions from all layers in the material, it cannot determine which layer is the surface and which is the interface, *i.e.* the same result will be obtained if the location of the surface and interface are swapped since each layer is weighted equally. On the other hand, while the surface-sensitive method can more precisely determine the surface valence, it will have little contribution from the interface, so the interface valence cannot accurately be determined. Therefore, by fitting the FY and TEY data simultaneously to the above model, we can determine both the surface and interface valence. In our fitting, the probing depths λ were set to 2.6 nm for TEY (Ruosi *et al.*, 2014) and 4 µm for FY (Henke *et al.*, 1993). The attenuation lengths λ_0 of the incoming X-rays were set to 4 µm for the Mn *K* edge and 140 nm for the Mn *L* edge (Henke *et al.*, 1993).

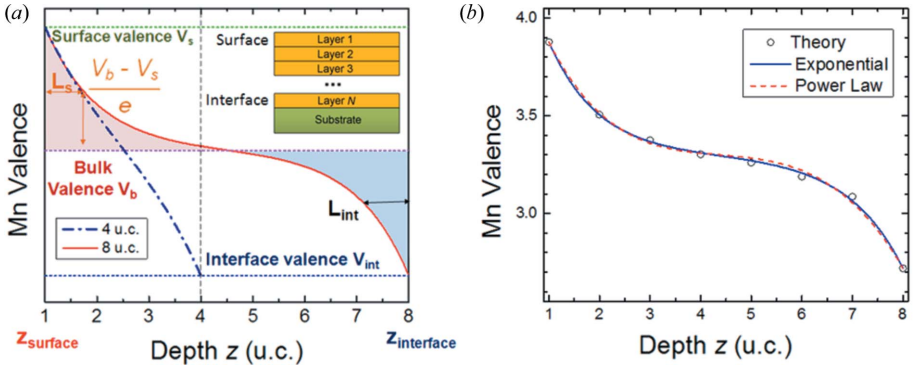

Figure 6
(*a*) Schematic of the variation of valence with depth. Curves are shown for sample thicknesses of 4 u.c. (dash-dot line) and 8 u.c. (solid line). Inset: diagram showing layer numbers of LSMO as a function of distance from the surface for a given film thickness. Here, $z = 1$ is taken to be the surface Mn layer. (*b*) Layer-by-layer variation of valence for material thickness of 8 u.c. The data points correspond to the valence determined by theoretical calculations and the blue and red curves show the exponential and power-law fits to the data, respectively.

Fitted results are shown in Fig. 4, as dashed curves. The model provides a reasonable fit to the experimental data. However, inspection of both the TB results presented here and previous density functional theory (DFT) calculations (Trappen *et al.*, 2018) indicate that the values for the surface and interface valences are not constant, as assumed by the model here. The physical reason for this change lies in the polar discontinuity of the LSMO/STO interface, as explained by Trappen *et al.* (2018). Our previous DFT calculations indicate that, as the sample thickness increases from one to four unit cells, the electric potential buildup caused by LSMO's polar layers begins to have an increasingly prominent effect which causes a charge redistribution. The effect stabilizes after roughly four unit cells, after which the surface and interface valence are approximately constant and the electric potential across the film is nearly zero. This change is also evident in the TB calculation results shown in Fig. 5, which show a similar thickness variation.

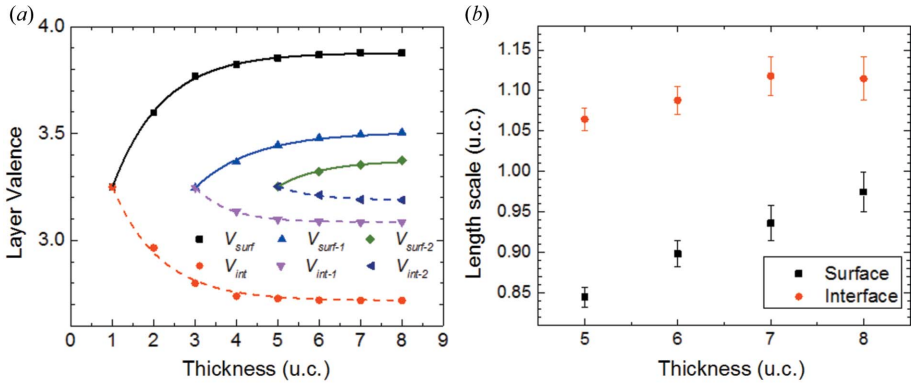

Figure 7
(*a*) Variation of the surface and interface-layer valence with thickness as predicted by theory. As each layer follows similar thickness-dependent trends, equations (2) and (3) were employed and the resulting dashed lines are shown. Here $V_{surf\text{-}n}$ ($V_{int\text{-}n}$) refers to the valence of the nth layer from the surface (interface). (*b*) Thickness dependence of the surface and interface-length scales, L_s and L_{int}, as determined by fitting the theoretical data in Fig. 4 to equation (1). Points below 5 u.c. have been omitted as there are a sufficient number of parameters to fit equation (1) exactly to the data, *i.e.* the error is zero.

In order to model this change in our own system, the thickness variation of the surface and interface valence (as well as layers near the surface and interface) was analyzed [Fig. 6(*a*), solid and dashed curves] and found to follow a saturating exponential trend of the form

$$V_{s,i}(t) = \gamma\left\{1 - \exp\left[-(t/L_{Vs,i})\right]\right\} + \delta. \quad (5)$$

Here, equation (5) represents two equations, one characterizing the variation of the surface valence V_s and one for the interface valence V_i. Similar to equation (1), the coefficients γ and δ are solved from the conditions that $V_s(1) = V_i(1) = V_{mono}$, $V_s(\infty) = V_{surf}$ and $V_i(\infty) = V_{int}$. They have the form

$$\gamma = \exp(1/L_{Vs})(V_{mono} - V_{surf}) + V_{surf}, \quad (6)$$

$$\delta = \exp(1/L_{Vs})(V_{surf} - V_{mono}). \quad (7)$$

The first condition reflects the fact that at 1 u.c. the surface is the interface, while the conditions at $t \rightarrow \infty$ indicate that the values of the surface and interface valence should saturate after some characteristic variation L_{Vi}, L_{Vs}.

The values of L_{Vi} and L_{Vs} determined by fitting the theoretical data shown in Fig. 7(*a*) were determined to be 1.1 u.c. for both the surface and interface valence, though we allowed these values to be parameters in our fitting of the experimental data. The length scales L_s and L_{int} schematically illustrated in Fig. 6 appear to increase slightly with sample thickness and potentially saturate; however, the overall variation is no more than approximately 0.2 u.c. (Fig. 7*b*). Therefore, in our fitting, we fixed the parameters L_s and L_{int} to be the same for all sample thicknesses. Results of the fit using the thickness-varying surface and interface valence are shown in Fig. 4 (solid lines). As can be seen, both solid and dotted fits provide nearly the same quality. However, as discussed further below, the error on the parameters is much lower using the thickness-varying model.

Fig. 8 shows a comparison between the layer-dependent valence obtained from the two models, where the thickness-dependent surface and interface layers are either constant (dashed lines and open points) or not (solid lines and filled points). Besides the surface and interface-valence values, the profiles are quite similar. In fact, the agreement is within error for the larger sample thicknesses. The best-fit values for the surface and interface valence vary by approximately 0.1 for both models.

The plane-resolved valence obtained from the fit is compared with theory in Fig. 5. The trend indicated by the experimental fit generally follows the theoretical predictions, with a difference of 0.1–0.2 between the predicted and fitted

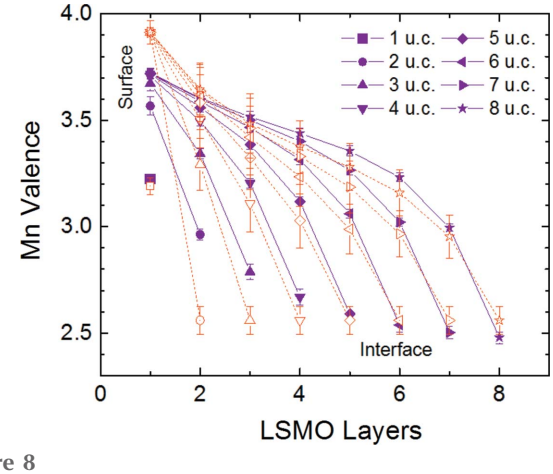

Figure 8
Comparison between the fitted layer-by-layer valence obtained from the model where the parameters do and do not vary with thickness (solid lines/solid points and dashed lines/open points, respectively).

surface and interface values. The length scales L_s and L_{int} vary from theory by about 1 u.c. and may be related to the presence of charge-transfer effects and oxygen vacancies (discussed by Trappen *et al.*, 2018) not considered by the TB model. The thickness variations L_{Vs} and L_{Vi} are quite similar to the trends predicted by the TB model, with the surface and interface valence saturating after 2–3 u.c. Additionally, incorporating this thickness variation provides good agreement with DFT calculations (Trappen *et al.*, 2018). While some small differences from the theoretical calculations are apparent, we find reasonable agreement between the model and theory and that the trends indicated by theory can be used to model the change in valence in this system. The calculations presented here and in our previous work indicate that the physics in several monolayer systems can differ substantially from thicker films because of strong contributions from surface and interface effects and the modeling presented here provides a way to account for this variation.

4. Conclusion

We have presented a model based on theoretical calculations to determine the layer-by-layer variation of valence in thin-film materials. Our fit results indicate that, while the Mn valence in LSMO thin film is close to its expected bulk value in the central layers of the material, there is significant variation of the valence near surfaces and interfaces. This variation is thickness dependent as well, and differs in film thicknesses of several monolayers from larger thicknesses. While the thickness-varying model presented here can be used to study thickness-dependent effects in ultrathin-film systems, the simpler model presented here could be used to study thicker films.

While this model has been used here to study the valence profile in LSMO thin films, the method discussed here is applicable to other systems where atomic valence is expected to influence the material properties and may also be extended to model depth-dependent magnetism using a combination of bulk and surface-magnetization measurements.

Acknowledgements

The authors are grateful to Matthew A. Marcus and Alpha T. N'Diyae for useful discussions.

Funding information

This work was carried out at the Advanced Light Source, Lawrence Berkeley National Laboratory, Berkeley, CA, USA, whose operations are supported by the Director, Office of Science, Office of Basic Energy Sciences, US Department of Energy under Contract No. DE-AC02-05CH11231. The double-exchange-model simulation by Shuai Dong was supported by the NSFC (Nos. 11274060 and 51322206). Synchrotron and electron-microscopy measurements were supported by NSF (DMR-1608656). The layer-by-layer fit to experimental data was supported by the US Department of Energy, Office of Science, Office of Basic Energy Sciences under Award Number DE-SC0016176.

References

Alonso, J. M., Cortés-Gil, R., Ruiz-González, L., González-Calbet, J. M., Hernando, A., Vallet-Regí, M., Dávila, M. E. & Asensio, M. C. (2007). *Eur. J. Inorg. Chem.* **2007**, 3350–3355.
Bals, S., Tirry, W., Geurts, R., Yang, Z. & Schryvers, D. (2007). *Microsc. Microanal.* **13**, 80–86.
Batzill, M. (2006). *Sensors*, **6**, 1345–1366.
Bertacco, R., Contour, J. P., Barthélemy, A. & Olivier, J. (2002). *Surf. Sci.* **511**, 366–372.
Björck, M. & Andersson, G. (2007). *J. Appl. Cryst.* **40**, 1174–1178.
Butler, C. J., Yang, H.-H., Hong, J.-Y., Hsu, S.-H., Sankar, R., Lu, C.-I., Lu, H.-Y., Yang, K. H., Shiu, H.-W., Chen, C.-H., Kaun, C.-C., Shu, G.-J., Chou, F.-C. & Lin, M.-T. (2014). *Nat. Commun.* **5**, 4066.
Dong, S., Zhang, X., Yu, R., Liu, J.-M. & Dagotto, E. (2011). *Phys. Rev. B*, **84**, 155117.
Duba, A. & Nicholls, I. A. (1973). *Earth Planet. Sci. Lett.* **18**, 59–64.
Egerton, R. F. (2009). *Rep. Prog. Phys.* **72**, 016502.
Eisebitt, S., Böske, T., Rubensson, J.-E. & Eberhardt, W. (1993). *Phys. Rev. B*, **47**, 14103–14109.
Frazer, B. H., Gilbert, B., Sonderegger, B. R. & De Stasio, G. (2003). *Surf. Sci.* **537**, 161–167.
Gerber, O., Pichon, B. P., Ulhaq, C., Grenèche, J.-M., Lefevre, C., Florea, I., Ersen, O., Begin, D., Lemonnier, S., Barraud, E. & Begin-Colin, S. (2015). *J. Phys. Chem. C*, **119**, 24665–24673.
Gilbert, B., Frazer, B. H., Belz, A., Conrad, P. G., Nealson, K. H., Haskel, D., Lang, J. C., Srajer, G. & De Stasio, G. (2003). *J. Phys. Chem. A*, **107**, 2839–2847.
Groot, F. M. F. de & Kotani, A. (2008). *Core Level Spectroscopy of Solids*, 1st ed. New York: Taylor and Francis.
Henke, B. L., Gullikson, E. M. & Davis, J. C. (1993). *At. Data Nucl. Data Tables*, **54**, 181–342.
Holmes, A. T., Jaccard, D. & Miyake, K. (2007). *J. Phys. Soc. Jpn*, **76**, 051002.
Khan, M. (2015). PhD thesis, Freien Universität Berlin, Germany.
Kim, D. H., Lee, E., Kim, H. W., Kolesnik, S., Dabrowski, B., Kang, C., Kim, M., Min, B. I., Lee, H., Kim, J.-Y. & Kang, J.-S. (2015). *Phys. Rev. B*, **91**, 075113.
Li, Z., Bosman, M., Yang, Z., Ren, P., Wang, L., Cao, L., Yu, X., Ke, C., Breese, M. B. H., Rusydi, A., Zhu, W., Dong, Z. & Foo, Y. L. (2012). *Adv. Funct. Mater.* **22**, 4312–4321.
Manceau, A., Marcus, M. A. & Grangeon, S. (2012). *Am. Mineral.* **97**, 816–827.
Pecher, K., McCubbery, D., Kneedler, E., Rothe, J., Bargar, J., Meigs, G., Cox, L., Nealson, K. & Tonner, B. (2003). *Geochim. Cosmochim. Acta*, **67**, 1089–1098.
Pellegrin, E., Tjeng, L. H., de Groot, F. M. F., Hesper, R., Sawatzky, G. A., Moritomo, Y. & Tokura, Y. (1997). *J. Electron Spectrosc. Relat. Phenom.* **86**, 115–118.
Pesquera, D., Herranz, G., Barla, A., Pellegrin, E., Bondino, F., Magnano, E., Sánchez, F. & Fontcuberta, J. (2012). *Nat. Commun.* **3**, 1189.
Ruosi, A., Raisch, C., Verna, A., Werner, R., Davidson, B. A., Fujii, J., Kleiner, R. & Koelle, D. (2014). *Phys. Rev. B*, **90**, 125120.
Seah, M. P. & Dench, W. A. (1979). *Surf. Interface Anal.* **1**, 2–11.
Thompson, A. C. (2009). *X-ray Data Booklet*, 3rd ed. Lawrence Berkeley Laboratory, Berkeley, CA, USA.
Trappen, R., Garcia-Castro, A. C., Tra, V. T., Huang, C.-Y., Ibarra-Hernandez, W., Fitch, J., Singh, S., Zhou, J., Cabrera, G., Chu, Y.-H., LeBeau, J. M., Romero, A. H. & Holcomb, M. B. (2018). Submitted.

Ufuktepe, Y., Akgül, G., Aksoy, F. & Nordlund, D. (2011). *X-ray Spectrom.* **40**, 427–431.
Wadati, H., Achkar, A. J., Hawthorn, D. G., Regier, T. Z., Singh, M. P., Truong, K. D., Fournier, P., Chen, G., Mizokawa, T. & Sawatzky, G. A. (2012). *Appl. Phys. Lett.* **100**, 193906.
Wang, Y., Niranjan, M. K., Janicka, K., Velev, J. P., Zhuravlev, M., Jaswal, S. S. & Tsymbal, E. Y. (2010). *Phys. Rev. B*, **82**, 094114.
Wormington, M., Panaccione, C., Matney, K. M. & Bowen, D. K. (1999). *Philos. Trans. R. Soc. A: Math. Phys. Engineering Sci.* **357**, 2827–2848.
Zhou, J., Tra, V. T., Dong, S., Trappen, R., Marcus, M. A., Jenkins, C., Frye, C., Wolfe, E., White, R., Polisetty, S., Lin, J.-Y., LeBeau, J. M., Chu, Y.-H. & Holcomb, M. B. (2015). *Appl. Phys. Lett.* **107**, 141603.